1

Introduction

1.1 Prologue

In classical seismological observation, the first task was to read P- and S-wave onsets and maximum amplitudes of earthquake seismograms registered at stations to determine the earthquake hypocenter and its magnitude. Those measurements are also useful for the study of the Earth medium structure. In the 1960s, recorded direct arrival signals were often clipped since the dynamic range of recording systems was small. A complementary method was proposed to estimate the magnitude of an earthquake by measuring the duration time from the P-wave onset until the seismogram amplitude falls to the ground noise level (e.g., Solov'ev, 1965; Tsumura, 1967).

In the USA, Aki (1969) proposed to estimate the source spectrum phenomenologically from the spectrum of coda waves following the clipped direct arrival, where the word "coda" means the tail part of a seismogram. In the ex-Soviet Union, Rautian and Khalturin analyzed multi-bandpass filtered seismograms of earthquakes for a wide range of frequencies and lapse times up to more than thousands of seconds in various regions. They found that coda amplitudes have a common decay curve at different epicentral distances. They proposed a method to estimate the source spectrum of an earthquake from the spectrum of coda waves (e.g., Rautian et al., 1978, 1981). Nikolaev (1975) studied the collapse of a seismic wavelet with increasing travel distance in relation to the degree of medium heterogeneity. In Japan, Tsujiura (1978) reported that bandpass-filtered coda waves of local earthquakes have a common decay curve independent of earthquake magnitudes and epicentral distances. Their studies have led to the gradual recognition of the term "coda" in the seismological community. Seismologists often classified seismogram envelope patterns of small earthquakes in relation to regional differences of their epicenters (e.g., Research Group for Aftershocks, 1971); however, the physical mechanisms of complex seismogram envelope formation were not yet clearly understood in those days.

https://doi.org/10.1017/9781009049535.002 Published online by Cambridge University Press

In 1975, Aki and Chouet (1975) proposed a theoretical model to explain the excitation of coda waves quantitatively based on the theory of scalar wave scattering in random media (Chernov, 1960). Their single back-scattering model predicts that the power spectrum of coda waves is a convolution of the source power spectrum, the inverse square of the lapse time as a geometrical factor, and the back-scattering coefficient. The back-scattering coefficient is related to the power spectral density function (PSDF) of the random fractional velocity fluctuations. It was the first use of the radar equation in seismology. They ignored phase information and dealt with wave energy density, that is, their model is the simplest type of radiative transfer theory (RTT). Their work was a breakthrough for studying the random inhomogeneity of the solid Earth medium.

Many moonquake seismograms registered by the Apollo seismic network were found to be spindle-like (Nakamura, 1977b), which also boosted the study of wave scattering and the synthesis of seismogram envelopes in highly heterogeneous media based on the diffusion model (Wesley, 1965).

In the mid-1970s, one of the authors (HS) was involved in seismological observation at the deep-borehole seismic station IWT of National Research Center for Disaster Prevention (NRCDP) (currently National Research Institute for Earth Science and Disaster Resilience (NIED)) in Japan. He routinely read the P- and S-wave onsets and the maximum amplitude of each seismogram recorded on a paper chart; however, many seismograms were clipped because the recording system had a small dynamic range. He was also asked to read the duration of coda waves t_{F-P} to estimate the magnitude of the earthquake (see Figure 1.1 (a)). In addition to P and S arrivals, complex wave trains appear between these direct arrivals and after the S arrival. Although their phases are complex, the variation of the amplitude envelope looks smooth and systematic. He also got to know that the acoustic and mass-density well-logs measured in the borehole exhibit random fluctuations superposed on the step-like structure (see Figure 1.1 (b)). Inspired by the coda model of Aki and Chouet (1975), he became interested not only in coda wave excitation but also in a wide variety of three-component velocity seismogram envelopes in relation to random heterogeneity.

There were a few number of literature discussing wave scattering in seismological fields in those days. However, since the 1960s, there have been many studies based on the RTT in various fields of physics: on the propagation of light/electromagnetic waves in outer space, in the turbulent atmosphere and clouds, and the acoustic wave propagation through the turbulent atmosphere and ocean. It would be interesting for readers to learn those developments from review works and textbooks (e.g., Foldy, 1945; Chernov, 1960; Furutsu, 1964; Tatarskii, 1971; Barabanenkov et al., 1971; Flatté et al., 1979; Rytov et al., 1989; Apresyan and Kravtsov, 1996; Ishimaru, 1997). These studies were gradually introduced in the

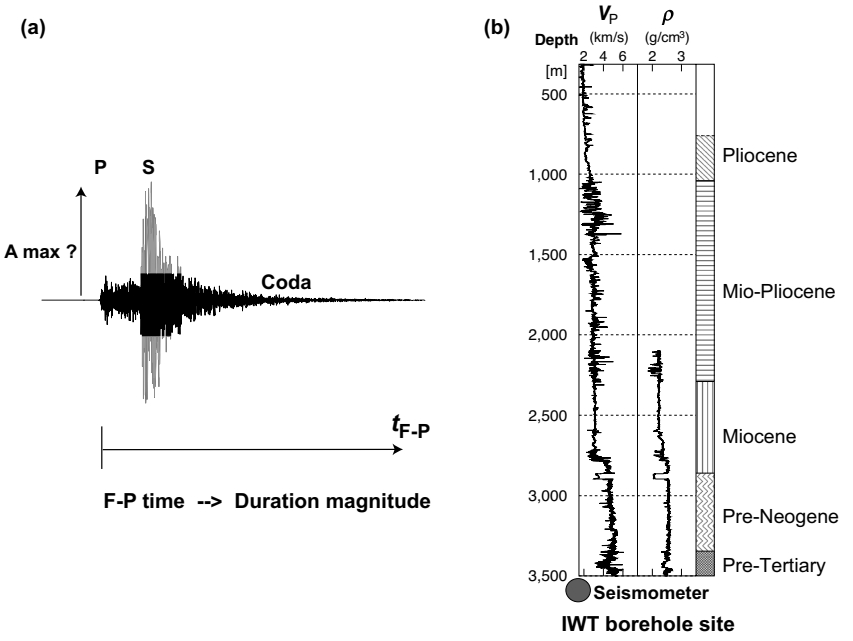

Figure 1.1 (a) Typical velocity seismogram of a small earthquake, where the direct wavelet is often clipped on a paper chart. (b) Acoustic and mass density well-logs of the IWT site of NRCDP (Shiomi et al., 1997, Fig. 3).

seismological community. Wu (1985) first proposed the use of the RTT, which can handle multiple scattering, for the study of coda excitation. Since then, original developments in the study of seismic wave scattering have been made in relation to the random heterogeneity of the solid Earth medium in the framework of RTT.

1.2 Recent Seismological Observation of Earthquakes

From the 1970s to the 1980s, seismic observation networks linked by telemetry were built in earthquake-prone countries around the world. In 1995, the Hyogo-ken Nanbu (Kobe) earthquake of M 7.3 took place in western Japan. That earthquake caused a major disaster and numerous deaths. Subsequently, NIED built "Hi-net," a nationwide network for real-time monitoring of seismic activity throughout Japan. The average separation of stations is as short as 20–25 km. Each station has a three-component velocity seismograph at the bottom of a borehole. The seismograph has a flat response to the ground velocity for frequencies higher than 1 Hz. The digital telemetry system drastically broadened the dynamic range of the whole seismological observation system.

https://doi.org/10.1017/9781009049535.002 Published online by Cambridge University Press

1.2.1 Coda Waves

Time Traces

The Hi-net array allows us to study how high-frequency seismic waves propagate. Even if it is difficult to analyze the phase information, we can see the spatiotemporal change in the mean squared (MS) velocity amplitude, which is proportional to the seismic energy density. Figure 1.2 (a) shows MS velocity–amplitude time traces of a local earthquake registered at various epicentral distances. MS velocity–amplitudes of coda waves decrease according to a common decay curve irrespective of epicentral distances. Figure 1.2 (b) shows MS velocity–amplitude time traces of different magnitude earthquakes registered at approximately equal epicentral distances, where each MS velocity–amplitude time trace is normalized by that at 100 s in lapse time measured from the origin time. This procedure is known as the coda normalized method. Coda normalized MS velocity amplitudes decrease according to a common decay curve irrespective of earthquake magnitudes.

Spatial Distributions

Changing the viewpoint, we show snapshots of the spatial distribution of seismic energy density in the 8–16 Hz band at different lapse times. Figure 1.3 (a) shows those of a crustal earthquake for a wide range of epicentral distances. The coda energy density is uniformly distributed inside of the S wavefront at a lapse time of 80 s. Figure 1.3 (b) shows those of an explosive P source in a volcanic field at small epicentral distances registered by a dense seismic array. Conversion scattering from P to S waves due to the strong heterogeneity effectively generates S waves, which concentrate near around the source. The excitation of coda waves strongly depends on the degree of medium heterogeneity.

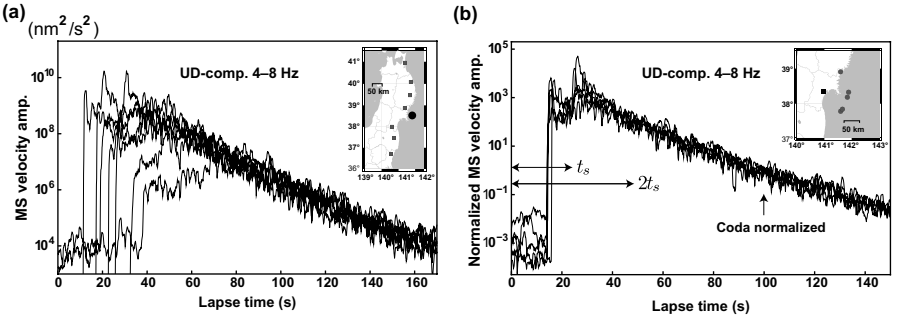

Figure 1.2 (a) Semi-log plot of MS velocity–amplitude time traces of an M 4.7 local earthquake (closed circles in the inset) registered at different stations (closed boxes). (b) Semi-log plot of coda normalized MS velocity–amplitude time traces of different magnitude earthquakes (M 4.0–4.6, closed circles in the inset) registered at nearly equal epicentral distances (closed box), where Hi-net data of NIED are used.

https://doi.org/10.1017/9781009049535.002 Published online by Cambridge University Press

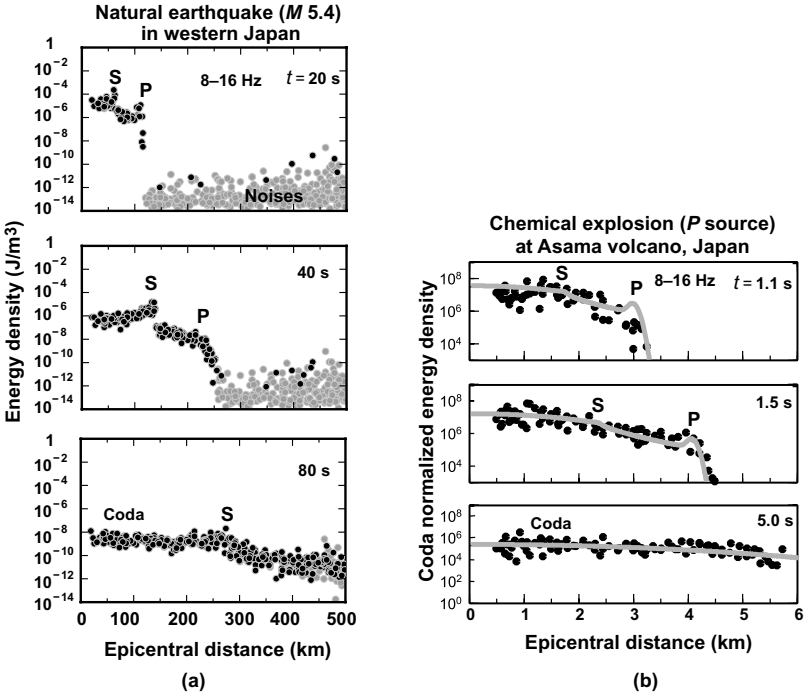

Figure 1.3 Semi-log plot the spatial distribution of seismic energy density at different lapse times measured from the origin time. (a) For a crustal earthquake in western Japan, where Hi-net data of NIED are used. S-wave radiation is dominant. (b) For a chemical explosion (P source) at Asama volcano, Japan, where gray curves are best-fit isotropic scattering model solutions (Yamamoto and Sato, 2010, Fig. 4).

1.2.2 Envelope Broadening

Another scattering effect is the envelope broadening of a seismic wavelet. Figure 1.4 (b) shows the temporal change of the root mean squared (RMS) velocity seismogram amplitudes at different epicentral distances, where the earthquake epicenter and stations are shown in Figure 1.4 (a). The apparent duration of the S wavelet is broadened with increasing epicentral distance.

Figure 1.5 (a) shows a typical velocity seismogram of a small earthquake with its bandpass-filtered RMS amplitude traces, where t_p is the peak delay time from the S onset. Figure 1.5 (b) plots t_p against hypocentral distance for many earthquakes in the magnitude range from 2.3 to 5.5. Although the scatter is significant, the peak delay increases with increasing hypocentral distance, as shown by the regression line (white) in each frequency band.

The envelope broadening with increasing travel distance can be explained by the accumulation of narrow-angle ray bending around the principal ray direction due to

https://doi.org/10.1017/9781009049535.002 Published online by Cambridge University Press

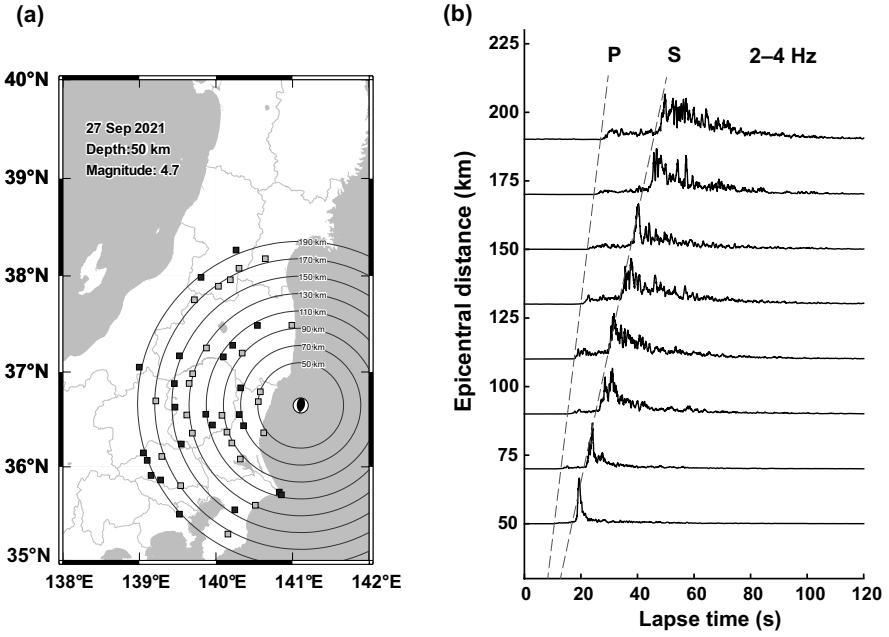

Figure 1.4 (a) Hi-net stations of NIED (boxes) and an M 4.7 earthquake in the eastern Honshu, Japan. (b) RMS amplitudes of stacked transverse-component velocity seismograms (2–4 Hz band) at different epicentral distances, where each trace is normalized by the maximum peak value.

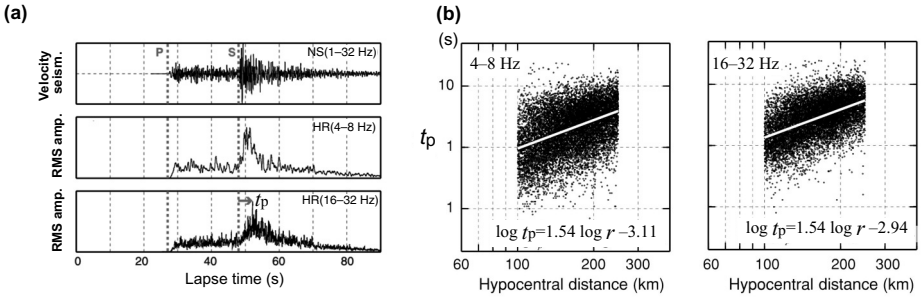

Figure 1.5 (a) Velocity seismogram (NS comp.) and bandpass-filtered RMS amplitude time traces (horizontal component) of a small earthquake in NE-Honshu, Japan, where t_p is the peak delay from the S onset. (b) Log-log plot of peak delay time t_p versus hypocentral distance r (Takahashi et al., 2007, Figs. 2 and 3).

slowly varying velocity fluctuations (Sato, 1989; Obara and Sato, 1995; Saito et al., 2002b). Regional studies in the Japan arc revealed that the gradient of peak delay time against travel distance depends on frequency. When S wavelets propagate

https://doi.org/10.1017/9781009049535.002 Published online by Cambridge University Press

beneath Quaternary volcanoes, long delays are observed at stations on the back-arc side (Takahashi et al., 2007).

1.3 Developments in Theory and Observation

Since the late 1970s, significant advances have been made in the study of seismic wave propagation and scattering in random heterogeneities mainly on the basis of the RTT. Aki (1982, 1984) reviewed the research status in the early 1980s, and Aki (1991) and Sato (1991) summarized the discussion held at the 1989 IASPEI meeting in Istanbul. In the following, we enumerate developments in theory and observation up to recent years, where detailed explanation of terms related to scattering will be given in Chapter 2.

- **Modeling and analysis of coda waves:** Aki and Chouet (1975) proposed the single back-scattering model for synthesizing the coda-wave envelope following the S arrival in random media. The single isotropic scattering model was developed by Kopnichev (1975) and Sato (1977); later the multiple isotropic scattering model was developed (Zeng et al., 1991; Shang and Gao, 1988; Sato, 1993; Paasschens, 1997). The isotropic scattering coefficient g_{iso} of S waves and coda attenuation factor Q_c^{-1} have been measured from the coda analysis of local earthquakes in various regions of the world (e.g., Rautian and Khalturin, 1978; Jin and Aki, 1988; Matsumoto and Hasegawa, 1989; Cichowicz and Green, 1989; Nishigami, 2000; Yoshimoto and Jin, 2008; Lee and Sato, 2006; Jin and Aki, 2005; Havskov et al., 2016; Mitra et al., 2022). Measurements of those quantities were also done for moonquakes and Martian events (Gillet et al., 2017; Menina et al., 2021). S-wave g_{iso} values of granite and gabbro rock samples were measured at an ultrasonic frequency of 1 MHz (Sato, 2019a; Zhou et al., 2021).

  Wu and Aki (1988) used the RTT for the measurement of scattering attenuation and intrinsic absorption from coda envelope analysis. Hoshiba et al. (1991) proposed the multiple lapse-time window analysis based on the time-dependent RTT, which is a powerful tool for the simultaneous measurement of g_{iso} and intrinsic absorption Q_I^{-1} from the entire S-wave seismogram envelopes of local earthquakes (e.g., Fehler et al., 1992; Hoshiba, 1993; Mayeda et al., 1992; Feustel, 1998; Chung et al., 2009; Carcolé and Sato, 2010; Rachman and Chung, 2016; Eulenfeld and Wegler, 2017; Shito et al., 2020; Calvet et al., 2023). A summary of reported S-wave g_{iso} values will be shown in Figure 1.6.
- **Coda normalization method:** The uniform distribution of coda energy density at a long lapse time is the observational base for the coda normalization method. It is a valuable tool for measuring site amplification factor, attenuation factor,

https://doi.org/10.1017/9781009049535.002 Published online by Cambridge University Press

and source radiation energy (e.g., Rautian and Khalturin, 1978; Tsujiura, 1978; Aki, 1980a; Phillips and Aki, 1986; Yoshimoto et al., 1993; Kato et al., 1995; Fehler and Sato, 2003; Takahashi et al., 2005).

- **Modelling of Rayleigh-wave coda:** The isotropic scattering model was extended to the propagation of a Rayleigh wavelet around the spherical surface of the solid Earth (Sato and Nohechi, 2001; Maeda et al., 2003). Analyzing Rayleigh waves, Sato and Nishino (2002) estimated $g_{iso} \approx 2 \times 10^{-6}\,\mathrm{km}^{-1}$ for 0.0056–0.0125 Hz. Maeda et al. (2006) interpreted that higher-mode Rayleigh waves are uniformly distributed at a long lapse time due to large velocity dispersion and scattering. They dominate over the fundamental mode Rayleigh waves because of small intrinsic attenuation in the lower mantle. Applying the isotropic scattering model to Rayleigh coda waves excited by a mars-quake, Onodera et al. (2023) estimated $g_{iso} = 3.4 \times 10^{-4}$–$5.7 \times 10^{-3}\,\mathrm{km}^{-1}$ for 0.05–0.09 Hz.
- **Scattering attenuation:** To compensate for the coda excitation, scattering attenuates the direct wave amplitude in random media. Since the 1980s, scattering has come to be recognized as one of the physical mechanisms of attenuation. There have been various approaches to evaluate scattering attenuation in random media (e.g., Aki, 1980b; Wu, 1982; Sato, 1982a; Dubendorff and Menke, 1986; Shapiro and Kneib, 1993; Roth and Korn, 1993; Fang and Müller, 1996) and those in cracked media (Kikuchi, 1981; Yamashita, 1990; Benites et al., 1992; Kawahara and Yamashita, 1992; Guo et al., 2018; Sato, 2021).
- **Finite difference (FD) simulation of waves in random media:** FD simulations have been used for the synthesis of coda waves in random media (e.g., Frankel and Clayton, 1986; Frankel and Wennerberg, 1987). Furumura and Kennett (2005) synthesized wave propagation through the oceanic slab composed of a random layer to explain intensity anomalies in northern Japan.
- **Envelope broadening with increasing travel distance:** The apparent duration of the S wavelet of a regional earthquake is broadened with increasing travel distance in slowly varying random velocity fluctuations. Assuming Gaussian-type random media, Sato (1989) synthesized the envelope broadening by the Markov approximation theory based on the parabolic approximation. The Markov approximation was extended to the case of von Kármán-type random media (Saito et al., 2002b; Takahashi et al., 2007; Saito et al., 2008), and that for a vector wavelet was also developed (Sato, 2006; Sawazaki et al., 2011). The synthesized envelopes were compared with FD simulation results (e.g., Fehler et al., 2000; Saito et al., 2003; Korn and Sato, 2005; Emoto et al., 2010, 2012). Envelope broadening was measured in various areas in the world (e.g., Tripathi et al., 2010; Petukhin and Gusev, 2003; Calvet et al., 2013).
- **Synthesis of full-seismogram envelope in random media:** Even if random media are statistically homogeneous and isotropic, the Born approximation

https://doi.org/10.1017/9781009049535.002 Published online by Cambridge University Press

predicts that the scattering pattern of scalar waves is anisotropic depending on frequency. Monte Carlo (MC) simulations have often been used to solve the radiative transfer equation (RTE) for a given anisotropic scattering coefficient (e.g., Gusev and Abubakirov, 1987; Hoshiba, 1991; Hoshiba et al., 1991; Yoshimoto, 2000).

The development of vector wave scattering in random elastic media was done by using the Born approximation (Sato, 1984; Wu and Aki, 1985). Sato (1984) synthesized three-component RMS velocity-seismogram envelopes of a small earthquake based on the single scattering approximation. Several theoretical approaches to deriving the RTE have been proposed (e.g., Turner and Weaver, 1994; Ryzhik et al., 1996; Margerin et al., 2000; Margerin, 2005). Przybilla and Korn (2008) synthesized vector wave envelopes using MC simulations and then validated the accuracy by comparing with FD simulation results. Takeuchi (2016) developed the differential MC method that can simultaneously compute synthetic envelopes and their partial derivatives with respect to structural parameters, which reduces the required CPU time.

- **Measurement of the PSDF of random velocity fluctuations:** The PSDF of the random fractional velocity fluctuations was measured from the frequency dependence of the S-wave envelope broadening (e.g., Obara and Sato, 1995; Saito et al., 2005; Takahashi et al., 2009; Kubanza et al., 2006; Ugalde, 2013). Using the MC simulation, Sens-Schönfelder et al. (2009) analyzed Lg-wave excitation and blockage in a laterally inhomogeneous medium. Analyzing S and S-coda waves registered by ocean bottom seismometers, Takemura et al. (2023) estimated the random structure beneath the ocean. Combining deterministic and statistical structures, Sanborn et al. (2017) synthesized high-frequency vector seismograms. There were not only measurements of medium heterogeneity of the lithosphere but also those of the mantle and the CMB region from tele-seismic P-wave envelope analysis (e.g., Cormier, 1995; Margerin and Nollet, 2003; Margerin and Nolet, 2003; Poupinet and Kennett, 2004; Shearer and Earle, 2004; Shearer, 2015). From the fluctuation analysis of log-amplitude and travel time of tele-seismic P waves recorded by the USArray, Cormier et al. (2022) stochastically inverted for the precise depth variation of the RMS fractional velocity fluctuation in the mantle. A summary of reported PSDF measurements will be shown in Figure 1.7.
- **Retrieval of Green's function of the wave equation from coda waves and microseisms:** We can consider that late coda waves of local earthquakes are in the equipartition state (Weaver, 1982; Hennino et al., 2001). There have been developments in coda interferometry, which is the retrieval of Green's function of the wave equation from the cross-correlation analysis of coda waves or microseisms registered at distant stations (e.g., Campillo and Paul, 2003; Snieder,

https://doi.org/10.1017/9781009049535.002 Published online by Cambridge University Press

2004; Curtis et al., 2006; Sato, 2009; Wapenaar et al., 2010). The solution of the RTE is used as the sensitivity kernel for imaging the distribution of scatterers (Pacheco and Snieder, 2006; Obermann et al., 2013).

- **Temporal changes in coda characteristics:** The temporal changes in Q_c^{-1} and g_{iso} have been reported in association with major earthquake occurrences and volcanic eruptions (e.g., Fehler et al., 1988; Jin and Aki, 1986, 1989; Gusev and Lemzikov, 1985; Sato, 1987, 1988b; Hiramatsu et al., 2000; Jin et al., 2004; Aki, 2009).

1.4 Recent Measurements of Random Velocity Inhomogeneities

1.4.1 Isotropic Scattering Coefficient of S waves

In the framework of the RTT, the isotropic scattering model is simple and mathematically tractable, where the isotropic scattering coefficient g_{iso} is a quantitative measure of scattering strength per unit volume (2.3a). It is equal to the reciprocal of the mean free path as used in the kinetic gas theory. The excitation of coda waves increases as the g_{iso} value increases. Since the late 1970s, the g_{iso} value of S waves has been measured in various areas of the world. The size of the medium sampled varies widely, from rock samples on the order of millimeters to the crust and mantle on the order of thousand kilometers.

Figure 1.6 plots the reported g_{iso} values of S waves against frequencies from 0.1 Hz to 1 MHz, where the appropriate intrinsic absorption Q_I^{-1} value is assumed

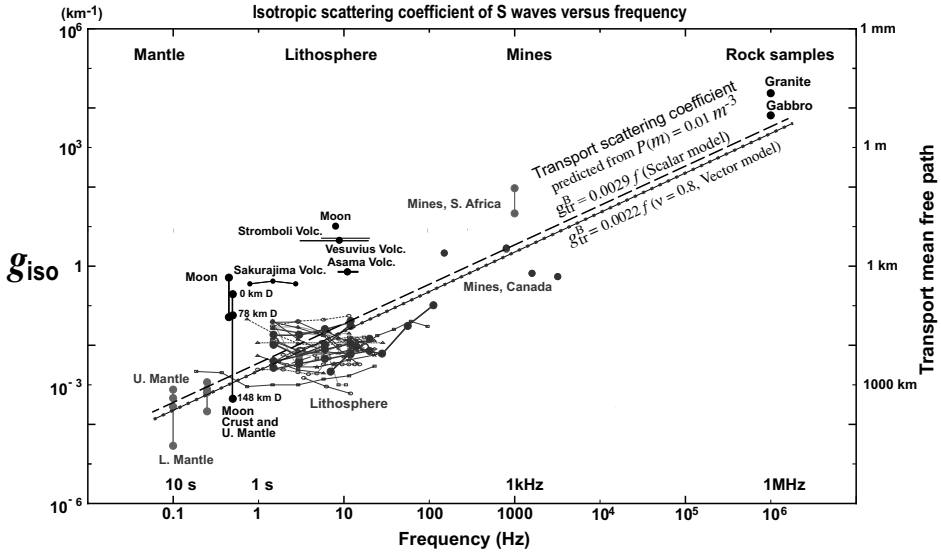

Figure 1.6 Log-log plot of reported isotropic scattering coefficients of S-waves measured in various regions of the solid Earth over a wide frequency range (modified from Sato, 2019a, Fig. 4, references therein).

https://doi.org/10.1017/9781009049535.002 Published online by Cambridge University Press

in each measurement. Although there is a large scatter of data, reported g_{iso} values linearly increase with increasing frequency. Dotted and dashed lines show the transport scattering coefficient g_{tr}^{B} predicted by the Born approximation (3.23c) from the spectral envelope of observed PSDFs of random fractional velocity fluctuations 0.01 m^{-3} (thick gray broken line in Figure 1.7), where m is the wavenumber (Sato, 2019a). We note that g_{tr}^{B} functions equivalently to g_{iso} in the diffusion regime (see Subsection 4.1.3). Reported g_{iso} values beneath volcanoes and on the Moon are much larger than those in the lithosphere, which indicates a possible scattering contribution of voids and cracks in addition to the random fractional velocity fluctuations.

1.4.2 PSDF of Random Fractional Velocity Fluctuations

As the most probable source of seismic wave scattering, we easily imagine random fractional velocity fluctuations, as seen in well-log data (see Figure 1.1 (b)). We assume that the inhomogeneous velocity is given by $V(\boldsymbol{x}) = V_0(1 + \xi(\boldsymbol{x}))$, where $\xi(\boldsymbol{x})$ is the fractional velocity fluctuation around the average velocity V_0. Using the PSDF of $\xi(\boldsymbol{x})$ is appropriate for characterizing the randomness statistically. There are several analytical models, among which the von Kármán-type PSDF (3.20a) is often used for practical analysis:

$$P(m) = \frac{8\pi^{\frac{3}{2}}\Gamma(\kappa + \frac{3}{2})\varepsilon^2 a^3}{\Gamma(\kappa)(1 + a^2m^2)^{\kappa+\frac{3}{2}}}, \tag{1.1}$$

where m, ε^2 and a^{-1} are the wavenumber, the MS fractional velocity fluctuation, and the corner wavenumber, respectively. The power-law decay characteristic $m^{-2\kappa-3}$ at large wavenumbers is preferable to the Gaussian-type PSDF with a fast drop-off.

Various measurements of P- and S-wave velocity fluctuations have been conducted on different portions of the solid Earth:

- Photo-scan of small rock samples (e.g., Sivaji et al., 2002; Fukushima et al., 2003)
- Well logs in boreholes (e.g., Suzuki et al., 1981; Wu et al., 1994; Holliger, 1996; Shiomi et al., 1997)
- Seismic array analysis (e.g., Aki, 1973; Capon, 1974; Powell and Meltzer, 1984; Flatté and Wu, 1988; Cormier et al., 2020, 2022)
- Envelope analysis of seismograms based on the RTT: cross-hole experiments (da Silva et al., 2018) local and regional earthquakes (e.g., Yoshimoto et al., 1997b; Petukhin and Gusev, 2003; Hock et al., 2004; Saito et al., 2005; Przybilla et al., 2009; Sens-Schönfelder et al., 2009; Emoto et al., 2017; Takahashi et al., 2009; Calvet and Margerin, 2013; Kobayashi et al., 2015; Sanborn et al., 2017;

https://doi.org/10.1017/9781009049535.002 Published online by Cambridge University Press

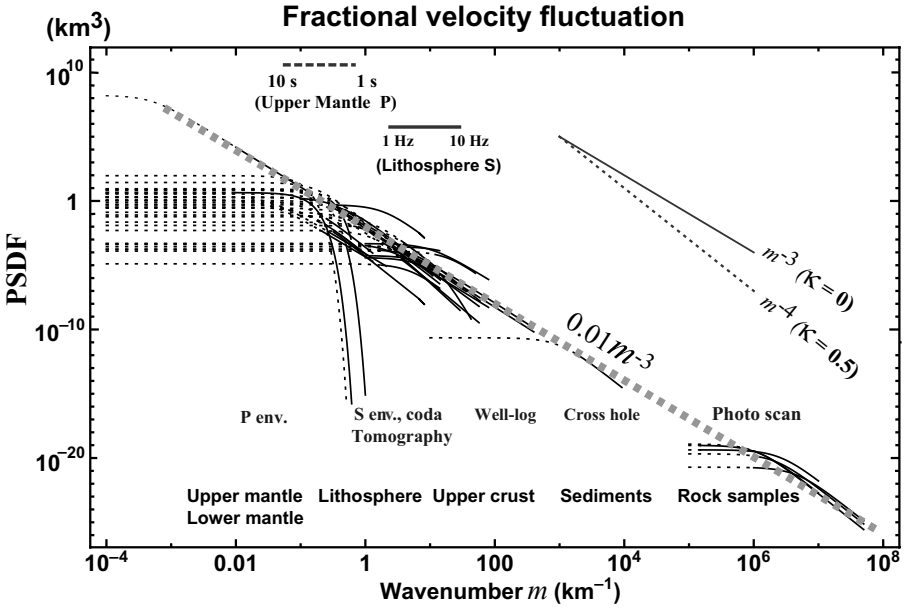

Figure 1.7 Log-log plot of reported PSDFs of the fractional velocity fluctuations of the solid Earth over a wide wavenumber range (Sato, 2019b, Fig. 9, references therein).

Morioka et al., 2017; Wang and Shearer, 2017); and teleseismic events (e.g., Cormier, 1999; Margerin and Nolet, 2003; Shearer and Earle, 2004; Mancinelli et al., 2016b)

- Velocity tomography (e.g., Chevrot et al., 1998; Nakata and Beroza, 2015)
- FD simulation (e.g., Furumura and Kennett, 2005; Takemura et al., 2023)

Figure 1.7 plots reported PSDF measurements against wavenumber m across a wide range of wavenumbers in various portions of the solid Earth. In most cases, random media are assumed to be isotropic and von Kármán type.

- Each PSDF is proportional to $m^{-3\sim-4}$ at wavenumbers higher than each corner, and many of them show the power-law decay close to m^{-3}.
- The reported ε values are of the order of 0.01~0.1 in the crust and the upper mantle, smaller in the lower mantle, and larger beneath volcanoes.
- The reported corner wavenumber a^{-1} values are widely distributed; however, each one seems to be restricted by the dimension of the measurement system or the sample length. The number of measurements at wavenumbers smaller than a^{-1} is very few in each report.
- Roughly speaking, the spectral envelopes of these PSDFs are well approximated by a power-law decay curve $0.01\,m^{-3}$ (thick gray broken line) for a wide range of wavenumbers.

https://doi.org/10.1017/9781009049535.002 Published online by Cambridge University Press

Other Examples of Power-law Spectra in Geophysics

There are some examples having power-law spectra in geophysical fields. A good example is the fractal nature of various kinds of surface topographies: Sayles and Thomas (1978) reported the one-dimensional PSDF $P_1(m) \propto m^{-2}$ for wavelengths 10^{-5} m~10^{2} m; Brown and Scholz (1985) reported $P_1(m) \propto m^{-1.64\sim-3.36}$ for wavelengths 10^{-5} m~1 m, especially for the topography of natural rock surfaces and faults.

Another example is the Kolmogorov spectrum of the refractive index of weak turbulence air. The refractive index is the ratio of light velocity in a vacuum to that in the medium. The Kolmogorov spectrum is modified from the von Kármán-type with $\kappa = 1/3$ (e.g., Ishimaru, 1997, p. 360):

$$P_{Air}(m) \propto \frac{e^{-m^2/{k_m}^2}}{(m^2 + {k_M}^2)^{11/6}}. \tag{1.2}$$

The energy is introduced into the turbulence due to wind shear and temperature gradients in the input range ($m < k_M$); the kinetic energy of the eddies dominates over the dissipation due to viscosity, where the turbulence is isotropic, and the PSDF is proportional to $m^{-11/3}$ in the inertial subrange ($k_M < m < k_m$). The cascade physically produces the Kolmogorov spectrum in the turbulent flow of low-viscosity air: large eddies break up to form smaller eddies, which dissipate energy by viscosity; the dissipation of energy due to viscosity dominates over the kinetic energy in the dissipation range ($m > k_m$).

1.5 Chapter Structure

The main objective of this book is to introduce the mathematical basics of wave scattering in random media. Then, we provide the flowcharts and mathematics required to code the MC simulation programs for wavelet propagation in the framework of RTT. We put our focus on the spatiotemporal variation of energy density for impulsive radiation from a source in random media. Using simple model random media, we validate MC simulation results by comparison with analytic solutions of the RTE and the ensemble average of FD simulation results. Especially for the scalar wave case, the essential scheme is illustrated by the diagram in Figure 1.8. We hope that these studies using simple random media models will help in the development of MC simulations for more realistic random media models. Below is a brief summary of each chapter:

- Chapter 2 introduces the isotropic scattering model, which is mathematically tractable. We introduce the basic concepts of the probability density function (PDF) of scattering angles and the inverse transform sampling method for

https://doi.org/10.1017/9781009049535.002 Published online by Cambridge University Press

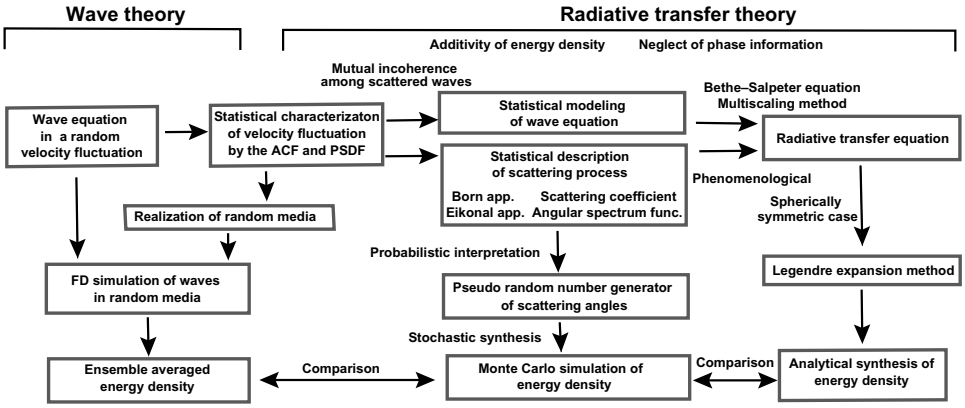

Figure 1.8 Basic scheme for the scalar wave case.

constructing the corresponding pseudo-random number generator (PRNG) of scattering angles. We then present the MC simulation of the space–time distribution of energy density for isotropic radiation from a point source, which is compared with the analytic solution of the RTE.

- Chapter 3 investigates the applicable range of the Born and Eikonal approximations for scalar wave scattering in random velocity fluctuations characterized by the PSDF. The Born approximation leads to the anisotropic scattering coefficient, which represents the directional scattering power per unit volume. The Eikonal approximation leads not only to the angular spectrum function (ASF) that governs narrow-angle ray bending but also to the travel distance fluctuation per travel time.
- Chapter 4 phenomenologically introduces the RTE of the directional distribution of energy density for a given anisotropic scattering coefficient of scalar waves in random media. We analytically solve the RTE by using the Legendre expansion for the isotropic radiation from a point source. Probabilistically interpreting the Born scattering coefficient and the Eikonal ASF for scalar waves, we construct the corresponding PRNGs of scattering angles, where the rejection sampling method is introduced. We then synthesize the space–time distribution of the energy density for isotropic radiation from a point source using the MC simulation and compare it with the analytic solution of the RTE.
- Chapter 5 presents the realization of random media for a given PSDF for the FD simulation of scalar wavelet propagation. We verify MC simulation results with the ensemble average of FD simulation results.
- Chapter 6 studies vector wave scattering in random elastic media. The Born approximation leads to PP, PS, SP, and SS scattering coefficients, from each of which we construct the corresponding PRNG of scattering angles. For a given

https://doi.org/10.1017/9781009049535.002 Published online by Cambridge University Press

PSDF, we synthesize three-component RMS velocity amplitude time traces for radiation from a point shear dislocation (PSD) source using MC simulations and compare them with the ensemble average of FD simulation results in realized random elastic media.

- In von Kármám-type random media, when the center wavenumber is higher than the corner wavenumber and the square of the phase shift across the correlation length is not small enough, the conventional Born approximation is not applicable. To overcome this difficulty, Chapter 7 presents an ongoing study of a hybrid MC simulation using the spectrum division method for scalar/vector wavelet propagation. Taking the center wavenumber as a reference, we divide the PSDF into two parts, then we serially use the Born wide-angle scattering for the high-wavenumber component and the Eikonal narrow-angle ray-bending and travel-distance fluctuation for the low-wavenumber component. Synthesized three-component RMS velocity amplitude time traces are compared with the ensemble average of FD simulation results in realized random elastic media for a given PSDF.
- In Epilogue, we discuss unsolved problems and possible developments in the future.

1.6 Mathematical Symbols

We briefly summarize some mathematical symbols frequently used in this book.

- A math symbol in bold $\boldsymbol{u}$ represents a vector. In 3D space, we often write $\boldsymbol{u} = (u_x, u_y, u_z)$ or (u_1, u_2, u_3) in Cartesian coordinates and $\boldsymbol{u} = (u_\theta, u_\phi, u_r)$ in spherical coordinates.
- The inner product of vectors is written as $\boldsymbol{a} \cdot \boldsymbol{b} = a_j b_j$, by using the Einstein summation convention.
- The symbol $d\boldsymbol{x} = dxdydz$ denotes an infinitesimal volume element in Cartesian coordinates, and $d\boldsymbol{x} = r^2 dr d\Omega$ in spherical coordinates, where $d\Omega = \sin\theta d\theta d\phi$ is a solid angle element.
- A hat and a tilde denote the Fourier transform with respect to time and space, respectively:

$$\widehat{f}(\boldsymbol{x}, \omega) = \int_{-\infty}^{\infty} dt\, e^{i\omega t} f(\boldsymbol{x}, t), \text{ and } \widetilde{f}(\boldsymbol{k}, t) = \iiint_{-\infty}^{\infty} d\boldsymbol{x}\, e^{-i\boldsymbol{k}\cdot\boldsymbol{x}} f(\boldsymbol{x}, t). \tag{1.3}$$

  Only in Section 4.2, a tilde refers to the spherical Bessel transform (4.9b).
- We define the inverse Fourier transform in 3D space and time using the plane-wave expansion:

https://doi.org/10.1017/9781009049535.002 Published online by Cambridge University Press

$$f(\boldsymbol{x},t) = \frac{1}{(2\pi)^4}\iiiint_{-\infty}^{\infty} d\omega\, d\boldsymbol{k}\, e^{i(\boldsymbol{k}\cdot\boldsymbol{x}-\omega t)}\,\widetilde{\widetilde{f}}(\boldsymbol{k},\omega),$$
$$\widetilde{\widetilde{f}}(\boldsymbol{k},\omega) = \iiiint_{-\infty}^{\infty} dt\, d\boldsymbol{x}\, e^{-i(\boldsymbol{k}\cdot\boldsymbol{x}-\omega t)}\, f(\boldsymbol{x},t). \tag{1.4}$$

- Convolution is symbolically written as follows:

$$A \otimes_{st} B \equiv \iiiint_{-\infty}^{\infty} d\boldsymbol{x}' dt'\, A(\boldsymbol{x}-\boldsymbol{x}', t-t') B(\boldsymbol{x}', t'),$$
$$A \otimes_{t} B \equiv \int_{-\infty}^{\infty} dt'\, A(t-t') B(t'),$$
$$A \otimes_{s} B \equiv \iiint_{-\infty}^{\infty} d\boldsymbol{x}'\, A(\boldsymbol{x}-\boldsymbol{x}') B(\boldsymbol{x}'). \tag{1.5}$$

- Angular brackets $\langle \cdots \rangle$ mean the average over the ensemble of random functions.
- The symbol $\mathrm{RG}_{\theta,\phi}$ means a PRNG of angles (θ, ϕ).

1.7 Recommended Reference Textbooks

The following textbooks are useful for reading this book:

- Mathematical Physics (Mathews and Walker, 1970; Arfken et al., 2013; Snieder and Kasper, 2015)
- Special Functions and Integral Formulas (Gradshteyn and Ryzhik, 2007; DLMF, 2022; Wolfram-Research, 2023)
- Scattering in Quantum Mechanics (Landau and Lifshitz, 2003)
- Numerical Simulation for Seismology (Moczo et al., 2014; Igel, 2017; Maeda et al., 2017)
- Earthquake Seismology (Aki and Richards, 2002; Shearer, 2019)
- Radiative Transfer Theory in Random miedia (Chandrasekhar, 1960; Chernov, 1960; Frisch, 1968; Barabanenkov et al., 1971; Ishimaru, 1997; Rytov et al., 1989; Apresyan and Kravtsov, 1996)
- Wave Propagation through Random Media in Geophysics (Flatté et al., 1979; Sato and Fehler, 2008; Sato et al., 2012; Shearer, 2015)

https://doi.org/10.1017/9781009049535.002 Published online by Cambridge University Press